23rd Australasian Fluid Mechanics Conference - 23AFMC
Sydney, Australia
4 – 8 December 2022
Paper No: AFMC2022-182

Transitional Boundary Layer Measurements in the University of Southern Queensland Hypersonic Wind Tunnel

Alister Webb[1*], Byrenn Birch[1], Fabian Zander[1], David Buttsworth[1]

[1] School of Engineering, the University of Southern Queensland, Toowoomba, QLD 4350, Australia
*mailto: alister.webb@usq.edu.au

Abstract

Surface pressure fluctuations on a sharp 7° half angle cone model at Mach 6 were measured in the University of Southern Queensland's hypersonic wind tunnel (TUSQ). High speed schlieren imagery showed instability wave-packets at approximately 250 kHz which was in agreement with the spectral analysis of the surface pressure fluctuations measured with PCB132 pressure sensors. These second mode instabilities exhibited the characteristic rope-like structure in the high-speed schlieren footage.

1 Introduction

To achieve controlled and sustained hypersonic flight, several gaps in fundamental knowledge must be addressed. One of these gaps is the fundamental understanding of the physical mechanisms responsible for the transition from a laminar to a turbulent boundary layer. The aerothermal heating of a vehicle and the skin friction drag are strong functions of the boundary layer state— turbulent boundary layers result in five-to-ten times the heating load and friction drag relative to laminar boundary layers. Therefore, by delaying the transition of a boundary layer, the thermal load and drag can be greatly reduced which greatly alleviates vehicle design constraints.

Vehicles designed for sustained hypersonic flight are typically slender, and boundary layer skin friction significantly affects the ballistic trajectory of such a vehicle. Over such a streamlined body, a laminar boundary layer results in less skin friction drag than a turbulent boundary layer. Should the boundary layers on a hypersonic vehicle be in a state such that the skin friction drag is asymmetric, it may not be possible to design sufficiently large control surfaces to provide the required trim for the vehicle (Batista and Kuehl, 2020). Hence, the ability to control the transition location is a crucial component of hypersonic vehicle design.

Most experimental data generated for the study of hypersonic transition is produced in conventional ground-testing facilities where the freestream disturbance levels are elevated relative to true flight which leads to premature transition. While 'low-noise' ground test facilities (e.g. BAM6QT at Purdue University, USA) offer a closer-to-flight disturbance level, such facilities are only capable of generating low-noise conditions at moderate Reynolds numbers. This means that conventional wind tunnels will continue to be used to characterise boundary layer transition on hypersonic vehicles (Marineau et al., 2018), but it is not appropriate to use simple correlations of transition location from ground-based experiments to design for flight conditions (Reshotko, 1976; Schneider, 2000). Instead, measurements of the boundary layer instabilities leading to transition are required in order to make meaningful progress towards understanding, and addressing, the transition problem (Laurence et al., 2016), with comparisons of these instability measurements in multiple facilities required (Marineau et al., 2018).

For relatively sharp bodies at hypersonic speeds, such as HIFiRE-1 (Kimmel et al., 2015), the laminar-to-turbulent transition is dominated by second-mode waves which manifest as convectively

amplified streamwise propagating disturbances with a distinctive acoustic signature (Fedorov et al., 2001). Because the second-mode dominates transition under typical hypersonic conditions, the laminar region can theoretically be extended by stabilization of the second-mode.

In this work, the pressure fluctuations beneath instability wave packets in a hypersonic boundary layer are investigated using a sharp-nose 7° half-angle cone at zero angle of attack in the University of Southern Queensland's hypersonic wind tunnel facility (TUSQ) at Mach 6. The pressure fluctuations are measured using PCB132B38 sensors which offer maximum bandwidth in excess of 1 MHz. The data acquired from these sensors are then analysed to investigate the second-mode instability. High-speed schlieren imaging (450,000 fps) is used to visualise the wall-normal density gradient.

2 Experimental Setup

2.1 Facility

The University of Southern Queensland's hypersonic wind tunnel (TUSQ) is a low enthalpy Ludwieg tube with free piston compression heating. It is the longest duration facility of its type in Australia and is capable of producing flow durations in excess of 200 ms (Buttsworth, 2010). When operated as a Ludwieg tube, supersonic and hypersonic flows can be produced with the following nozzles: Mach 2, Mach 4, Mach 6, and Mach 7. Additional supersonic flows are possible in an atmospheric blowdown configuration with Mach 3 and Mach 4.5 nozzles. The layout of the facility is shown in Figure 1.

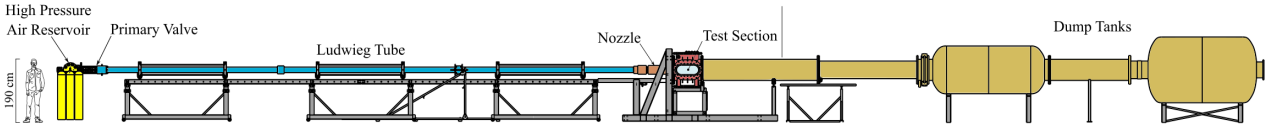

Figure 1. The general arrangement of TUSQ.

Operation of the facility begins with a light Mylar diaphragm separating the Ludwieg tube (barrel) and nozzle inlet. A 345 g piston is installed at the upstream end of the barrel. There are then three separate gas volumes: the high pressure (driver gas) reservoir; the barrel at ambient pressure and temperature; and the nozzle, test section, and dump tanks at a vacuum ($<$1 kPa). A run is initiated by opening a pneumatically actuated ball valve that separates the driver reservoir from the barrel. As the driver gas flows into the barrel, the piston is driven along the barrel, compressing the gas between it and the diaphragm.

The pressure of the gas ahead of the piston becomes high enough that it ruptures the Mylar diaphragm, accelerating the test gas through the nozzle and into the test section. The pressure in the barrel is measured by a PCB113A03 piezoelectric pressure transducer connected to a port 225 mm from the downstream end of the barrel. Triggering of the data acquisition system, optical diagnostics, and other hardware is reliant on this measurement. Nominal flow conditions for all experiments described herein are summarised in Table 1.

2.2 Model

The model is a 7° half angle cone, and is comprised of three sections: rear frustum, intermediate frustum, and nose tip. It is of similar design to those used in other facilities (Casper et al., 2016). The layout of the assembled cone is shown in Figure 2. Figure 3 shows the cone model installed on the model block in the test section. The base of the rear frustum features tapped holes for mounting

Table 1. Nominal flow conditions.

Stagnation pressure	1 MPa
Stagnation temperature	575 K
Static pressure	670 Pa
Static temperature	70 K
Static density	$0.034\,\mathrm{kg\,m^{-3}}$
Mach number	5.95
Unit Reynolds number	$7.17 \times 10^6\,\mathrm{m^{-1}}$

to a sting rod. The intermediate frustum is approximately 110 mm in length and is of monolithic construction. It features a threaded spigot on its small end for mounting nose tips, and a larger threaded hole in its base for mounting to the rear frustum. Three nose tips of different tip radii were manufactured, 0.05 mm, 0.1 mm, and 0.2 mm. The 0.2 mm radius tip was used for all experiments described herein. Each nose tip is approximately 75 mm long, with a tapped and counterbored hole in its base for mounting.

The rear frustum is comprised of two sections: the upper half is constructed from stainless steel (17-4PH), and the lower half is made of black Acetal (for future BL heat transfer studies using infrared imagery). The assembled frustum is hollow, having a stepped internal cavity to allow for cable access. The pressure sensors are installed with a silicone potting compound in inserts which are fastened from the inside of the housing. The model was fully assembled (including PCB inserts) and turned to final size ensure the junctions formed by mating surfaces would not produce a noticeable lip or step.

Pressure sensor locations are spaced approximately 32 mm apart on the cone surface, and all lie on the same azimuthal ray. The first sensor location is 205.8 mm from the nose tip, measured along the surface of the cone, and is designated as ‘A’. Sensor ports are lettered in alphabetical order from A to G towards the rear. Each sensor is mounted normal to the cone surface. Four PCB132B38 pressure sensors were installed in positions D–G for the present work.

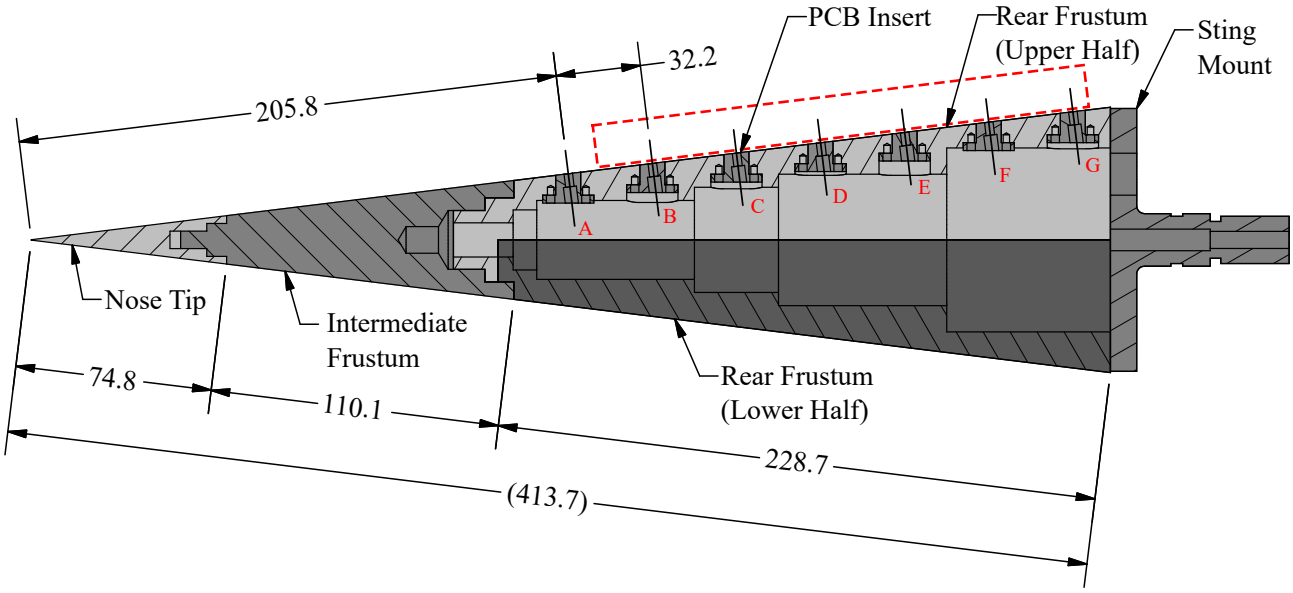

Figure 2. Schematic diagram of the cone model. The schlieren field of view (for Figures 5 and 6) is indicated by the red dashed rectangle.

2.3 Data Acquisition Systems

The data acquisition system is a National Instruments NI PXIe-1082 chassis with a PXIe-8861 controller and two pairs of PXI-6123 and PXIe-6124 multifunction I/O modules. The PXI-6123 has

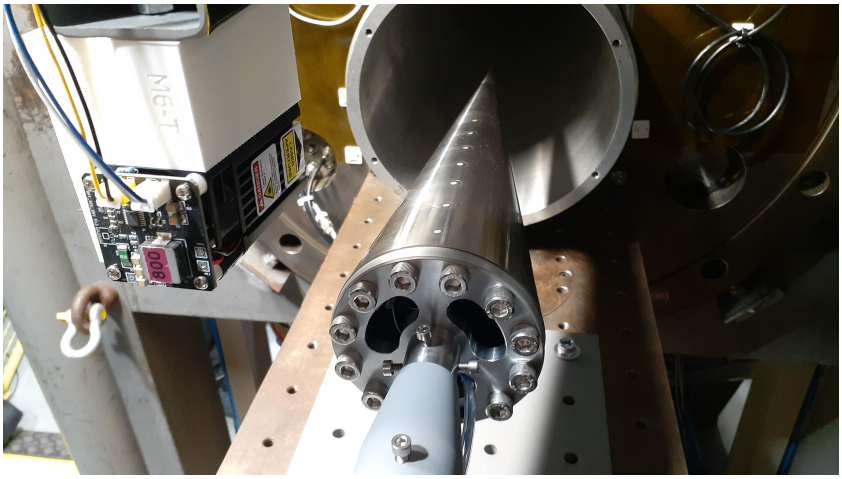

Figure 3. Cone model installed in the test section. Note the diaphragm rupture device above the model.

a maximum sample rate of 500 kHz, and was used for recording general facility diagnostics at a rate of 100 kHz. The PXIe-6124 has a much higher maximum sample rate of 4 MHz. The model pressure sensors were connected to one of the PXIe-6124 modules via a PCB Piezotronics 428C signal conditioner. They were then recorded with this module at a rate of 2 MHz, such that the PCB frequency data could be processed at up to 1 MHz.

The schlieren system is a z-type arrangement, consisting of five mirrors (three planar and two parabolic), a knife-edge, light source and high speed camera. The general layout of the system is shown in Figure 4. The light source is a Cavitar Cavilux UHS pulsed laser diode module, with the exposure time set to 20 ns. A Phantom TMX 7510 high speed camera (on temporary loan from Adept Turnkey and Vision Research) was used as the capture device at a rate of 450 000 fps and a resolution of 1280×128 px. The knife-edge and camera were both positioned parallel to the upper surface of the cone (rotated 7° from vertical) to capture wall-normal density gradients.

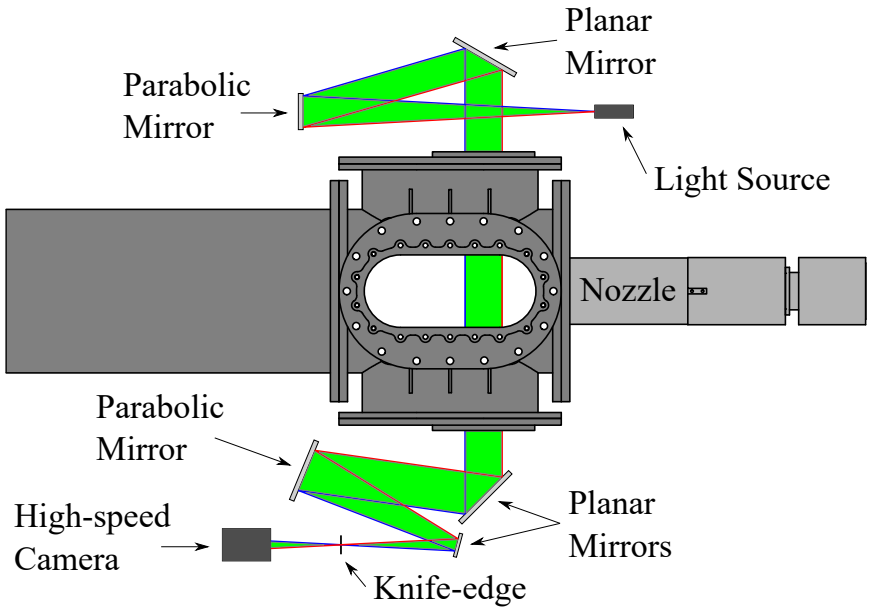

Figure 4. Schematic diagram of the schlieren system layout.

3 Results

3.1 Schlieren Imaging

The boundary layer is nominally laminar, however packets or spots of turbulence appear in varying sizes. Breakdown of the laminar boundary layer and transition to turbulence is also observed intermittently. The turbulent spots appear seemingly randomly, and are not of fixed height or length. They do not exhibit periodicity. Between some instances of turbulent spots, the laminar boundary layer exhibits rope-like structures characteristic of second mode instabilities.

In some cases turbulence was observed to originate from a spot or packet of rope-like structures. The effect was not consistent, some instances transitioned to turbulence within the schlieren window, whereas others were not observed to transition. The rope structures have an average wavelength of approximately 2.8 mm and are shown in Figure 5. Estimating the velocity from consecutive frames ($\delta x \approx 1.55$mm, $\delta t \approx 2.2\mu$s) at approximately 700 $\mathrm{m\,s^{-1}}$ yields a frequency of 242 kHz. This is within the range for second mode instabilities experimentally obtained by Chynoweth et al. (2017) and Stetson and Kimmel (1992) of 210 kHz to 300 kHz over similar geometry at Mach 6 and Mach 8 respectively.

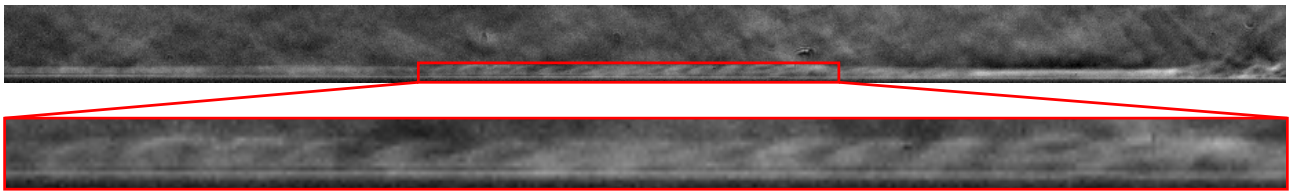

Figure 5. Rope structures formed in the boundary layer. Image contrast was adjusted and an average flowfield background subtraction was performed to emphasise the boundary layer.

Edge detection was performed on the schlieren images. The frames were windowed to remove high gradients at the model surface. A contrast adjustment was applied to the frame to minimise the increase in brightness in the x direction. A Logarithmic of Gaussian (LoG) edge detection was then performed on the adjusted frame, as well as two other contrast adjusted versions of the frame: high and low. The three edge detections were summed and Hampel filtered in y to remove detected areas of high gradient that are not in close proximity to the boundary layer.

A series of frames is shown in Figure 6. The edge detected frames show propagation of turbulent spots along the boundary layer, as well as their spatial and temporal growth. Growth in these localised regions occurred gradually at first, before a sudden onset of turbulence. Group velocity of the turbulent spots is estimated from consecutive frames at approximately 700 $\mathrm{m\,s^{-1}}$ — similar to the rope-like structures. The edge of the laminar boundary layer in Figure 6 can be seen to reside close to the red line which represents the (incompressible) empirical flat plate laminar boundary layer height. The height of the turbulent spots can also be seen to approach the blue line representing the turbulent case. The boundary layer heights were calculated based on free-stream unit Reynolds number, with distance from the model tip being the reference length scale.

3.2 Surface Pressure Measurements

The measured PCB132B38 signals were processed through a Hampel filter to remove spurious, high magnitude electrical noise induced spikes. In the interest of determining the ambient characteristics of the sensors, a Power Spectral Density (PSD) of the pre-flow data was computed.

As shown in Figure 7, the background noise in the pre-flow PSD was significant near 380 kHz and 870 kHz for all sensors. Noise levels for the two sensors in positions E and G were consistently larger than for D and F, especially near the aforementioned frequencies. Noise can also be observed from

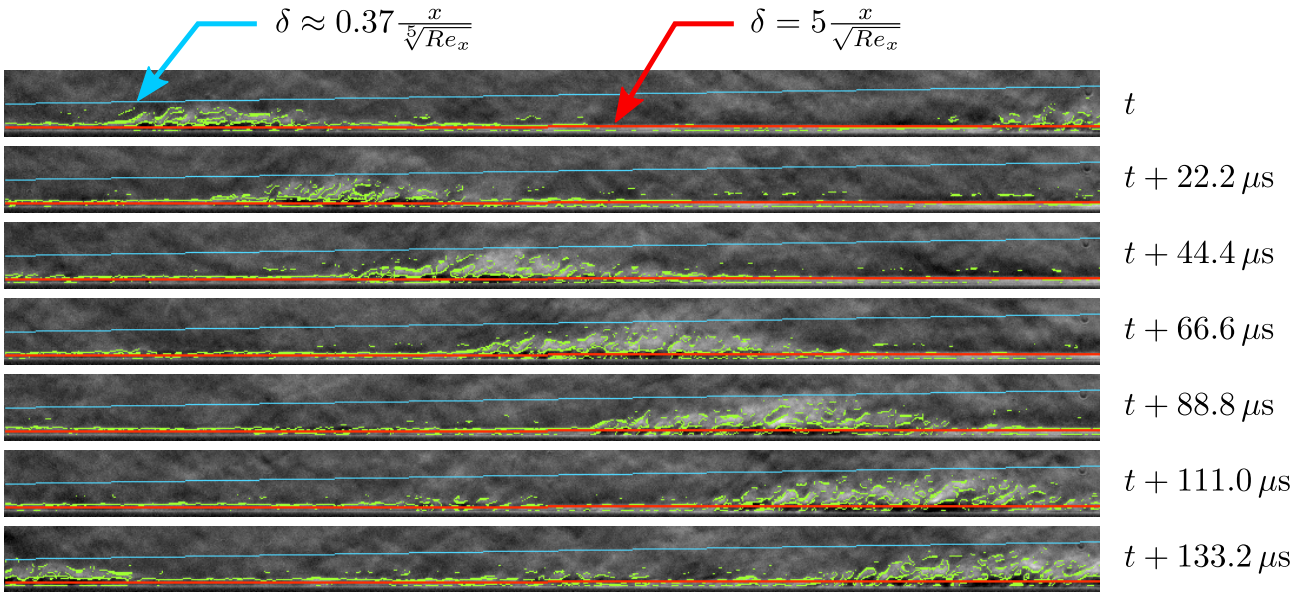

Figure 6. Seven frames of edge detected schlieren with adjusted contrast. Edge detection is shown in green, empirical boundary layer heights are shown in blue and red. Every tenth frame is shown to emphasise the development of the turbulent spot. Time step between each image is 22.2μs. Flow direction is from left to right.

500 kHz to 1000 kHz for these two sensors. Peaks seen at frequencies less than 100 kHz are attributed to electrical noise, frequencies in this range will not be used.

The remaining dataset was windowed to remove pre-flow and post-flow artefacts, including nozzle startup and flow termination. The PSD was then computed for the 20 ms period shown in Figure 8. Peaks in power can be seen between 200 kHz and 300 kHz before slowly declining to a local minimum near 600 kHz. This 200 - 300 kHz peak is consistent across all sensors, and decreases as the sensor moves downstream. It also coincides with the estimated frequency of the rope-like structures observed in the schlieren frames.

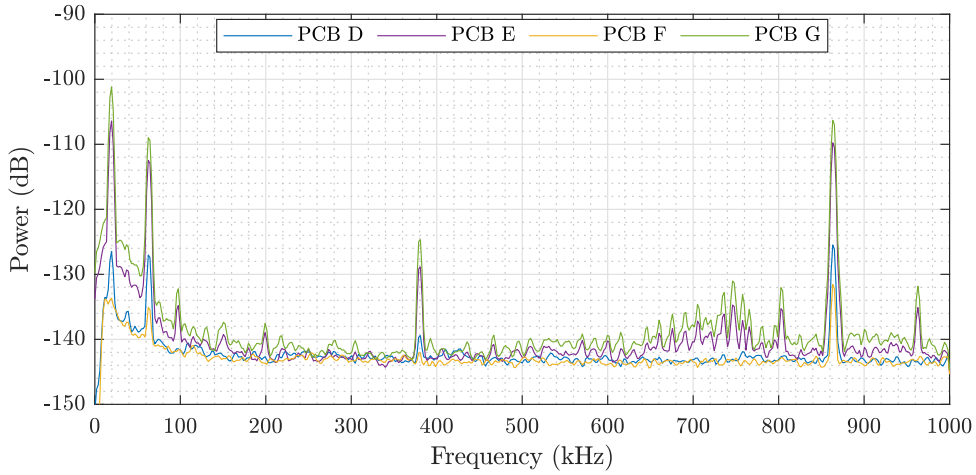

Figure 7. Pre-flow baseline PSD. The baseline in subsequent figures is calculated as the average of the PSD of each PCB.

Spectrograms were also produced for PCB D and E over the entire flow duration and are shown in Figure 9a, and Figure 9b respectively. Noise is more easily visible for PCB E here than in Figure 8, as it manifests as horizontal lines that span the width of the plot. High intensity is again visible at the 850 kHz peak and at frequencies lower than 100 kHz. Also visible is the high intensity in the 250 kHz range attributed to second mode instabilities. Flow start ($t = 0$) and termination ($t \approx 250$) can be seen

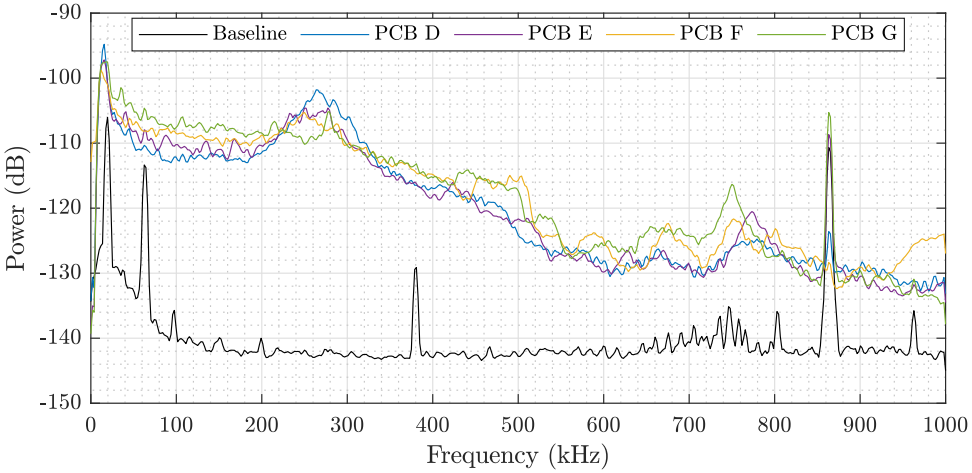

Figure 8. PSD of all sensors over a period of 30 ms to 50 ms after flow start.

as the sudden increase and decrease respectively in power density across all frequencies.

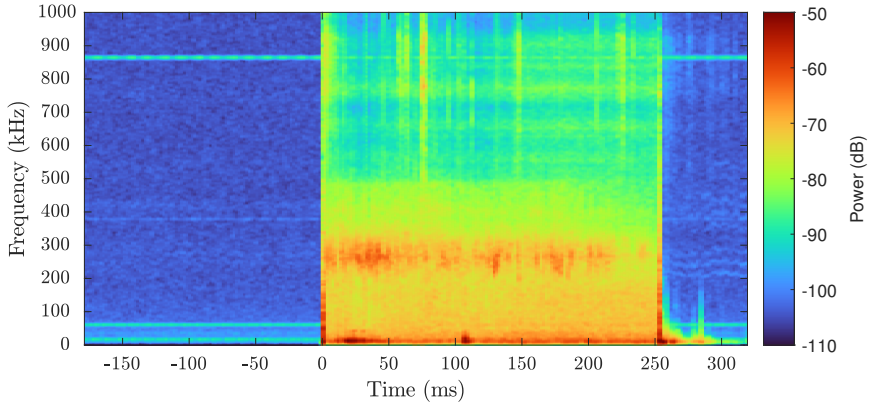

(a) Spectrogram of PCB D.

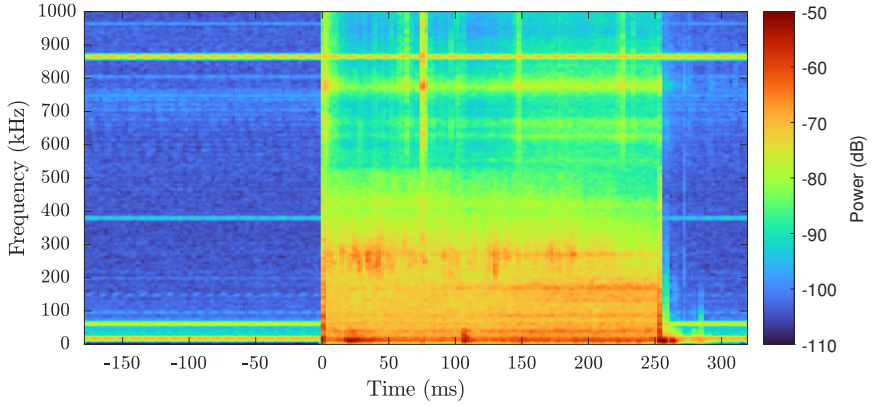

(b) Spectrogram of PCB E.

Figure 9. Spectrograms of PCBs D and E. The frequency peaks associated with noise are visible as horizontal lines spanning the width of the plot. Peaks are also visible during the flow time ($0 < t < 250$ ms) at 200 kHz–300 kHz.

4 Conclusions

Surface pressure fluctuations were measured for a sharp 7° half angle cone at Mach 6. Power spectral density calculations showed that frequencies in the range of 200 kHz to 300 kHz had the

largest intensity, indicating that it was the dominant frequency band in the boundary layer. Analysis of schlieren images indicated that second mode instabilities, imaged as their characteristic rope-like structures, possessed a frequency of approximately 250 kHz.

Acknowledgements

The authors would like to thank Lawrence Suryawinata from Adept Turnkey and Phil Taylor from Vision Research for loaning the Phantom TMX 7510 high speed camera used for the experiments. The model and instrumentation was funded from a USQ Research Capacity Building Grant. Alister Webb is supported by an Australian Government RTP scholarship.

References

Batista, A. and Kuehl, J. J. (2020). Local Wall Temperature Effects on the Second-Mode Instability. *Journal of Spacecraft and Rockets*, 57(3):580–595.

Buttsworth, D. R. (2010). Ludwieg Tunnel Facility with Free Piston Compression Heating for Supersonic and Hypersonic Testing. In *Proceedings of the 9th Australian Space Science Conference*, pages 153–162. National Space Society of Australia Ltd.

Casper, K. M., Beresh, S. J., Henfling, J. F., Spillers, R. W., Pruett, B. O., and Schneider, S. P. (2016). Hypersonic Wind-Tunnel Measurements of Boundary-Layer Transition on a Slender Cone. *AIAA Journal*, 54(4):1250–1263.

Chynoweth, B. C., Edelman, J., Gray, K., McKiernan, G., and Schneider, S. P. (2017). Measurements in the Boeing/AFOSR Mach-6 Quiet Tunnel on Hypersonic Boundary-layer Transition. In *47th AIAA Fluid Dynamics Conference*, page 3632.

Fedorov, A., Malmuth, N., Rasheed, A., and Hornung, H. (2001). Stabilization of Hypersonic Boundary Layers by Porous Coatings. In *39th Aerospace Sciences Meeting and Exhibit*. American Institute of Aeronautics and Astronautics.

Kimmel, R. L., Adamczak, D., Paull, A., Paull, R., Shannon, J., Pietsch, R., Frost, M., and Alesi, H. (2015). HIFiRE-1 Ascent-Phase Boundary-Layer Transition. *Journal of Spacecraft and Rockets*, 52(1):217–230.

Laurence, S. J., Wagner, A., and Hannemann, K. (2016). Experimental Study of Second-Mode Instability Growth and Breakdown in a Hypersonic Boundary Layer Using High-Speed Schlieren Visualization. *Journal of Fluid Mechanics*, 797:471–503.

Marineau, E. C., Grossir, G., Wagner, A., Leinemann, M., Radespiel, R., Tanno, H., Wadhams, T. P., Chynoweth, B. C., Schneider, S. P., Wagnild, R., and Casper, K. M. (2018). Compilation and Analysis of Second Mode Amplitudes on Sharp Cones in Hypersonic Wind Tunnels. In *2018 AIAA Aerospace Sciences Meeting*. American Institute of Aeronautics and Astronautics.

Reshotko, E. (1976). Boundary-Layer Stability and Transition. *Annual Review of Fluid Mechanics*, 8(1):311–349.

Schneider, S. (2000). Effects of High-Speed Tunnel Noise on Laminar-Turbulent Transition. In *21st Aerodynamic Measurement Technology and Ground Testing Conference*. American Institute of Aeronautics and Astronautics.

Stetson, K. and Kimmel, R. (1992). On Hypersonic Boundary-Layer Stability. In *30th aerospace sciences meeting and exhibit*, page 737.